Check for updates



APPLIED SCIENCES AND ENGINEERING

# At-home wireless sleep monitoring patches for the clinical assessment of sleep quality and sleep apnea

**Shinjae Kwon[1,2†], Hyeon Seok Kim[1,2†], Kangkyu Kwon[1,3], Hodam Kim[1,2], Yun Soung Kim[4], Sung Hoon Lee[1,3], Young-Tae Kwon[5], Jae-Woong Jeong[6], Lynn Marie Trotti[7], Audrey Duarte[8], Woon-Hong Yeo[1,2,9,10*]**

Copyright © 2023 The Authors, some rights reserved; exclusive licensee American Association for the Advancement of Science. No claim to original U.S. Government Works. Distributed under a Creative Commons Attribution NonCommercial License 4.0 (CC BY-NC).

**Although many people suffer from sleep disorders, most are undiagnosed, leading to impairments in health. The existing polysomnography method is not easily accessible; it's costly, burdensome to patients, and requires specialized facilities and personnel. Here, we report an at-home portable system that includes wireless sleep sensors and wearable electronics with embedded machine learning. We also show its application for assessing sleep quality and detecting sleep apnea with multiple patients. Unlike the conventional system using numerous bulky sensors, the soft, all-integrated wearable platform offers natural sleep wherever the user prefers. In a clinical study, the face-mounted patches that detect brain, eye, and muscle signals show comparable performance with polysomnography. When comparing healthy controls to sleep apnea patients, the wearable system can detect obstructive sleep apnea with an accuracy of 88.5%. Furthermore, deep learning offers automated sleep scoring, demonstrating portability, and point-of-care usability. At-home wearable electronics could ensure a promising future supporting portable sleep monitoring and home healthcare.**

## INTRODUCTION

Sleep is an integral part of the human life cycle, and its quality and duration play a critical role in physical, mental, and social health (*1*–*4*). As an increasing number of people recognize sleep as one of the essential factors in a healthy lifestyle, there has been rapid growth in sleep studies. The market size of the global sleep-related economy was $432 billion and is expected to grow to $585 billion by 2024 (*5*). Despite this elevated awareness, the average quality of a person's sleep has declined, and sleep disorder has become increasingly prevalent. Insufficient and poor sleep cause reduced labor productivity and increased mortality rates, leading to an economic loss of $411 billion in 2015, which is expected to grow to $467 billion in 2030 (*6*). Moreover, the American Association of Sleep Medicine (AASM) reports that one of the most prevalent sleep disorders, obstructive sleep apnea, afflicted 12% of the adult population in the United States and noted that 80% of them were left undiagnosed (*7*). The gold standard of sleep monitoring is polysomnography (PSG), but its various downsides impede its accessibility (*8*). PSG involves comprehensive measurements of patient physiological signals, including electroencephalograms (EEGs), electrooculograms (EOGs), electromyograms (EMGs), pulse oximetry, and more. Because of its complexity and difficulty in both hardware setups and data analysis, standard PSG is conducted at a specialized hospital with a certified sleep technologist, resulting in a time and cost burden. Moreover, because of the foreign environment with numerous hard-wired sensors and electronics placed throughout the body, patients may not have their natural sleep patterns, which can lead to inaccurate sleep quality assessment and disorder diagnosis.

Recent progress in the development of wearable devices has presented alternative ways for sleep monitoring at home (*8*, *9*). One of the widely used platforms is a wristband with integrated photoplethysmography and motion sensors. The convenience of the watch is attractive but fails to comprehensively cover the amount of physiological information needed for precise in-depth sleep analysis (*10*). EEG is often the most direct indicator of sleep stages and sleep disorders (*11*). Some headband devices can measure EEG and provide more precise sleep analysis (*12*–*16*). However, their bulky and rigid form factor discourages users from mounting them on their heads during sleep. Recent studies presented alternative form factors for sleep EEG measurement, such as those mounted either in or around the ear (*17*–*19*). Despite the improved usability, the alternative device locations suffer from poor signal quality and less accurate sleep analysis. For comfortable and seamless integration with our body for high-quality physiological monitoring, many recent works on developing soft wearable systems have been directed toward enhancing various aspects of epidermal electronics (*20*, *21*). Prior wearable devices show enhanced skin-contact quality by integrating the system on a soft substrate (*22*–*25*). However, the required membrane materials for these ultrathin devices limit the number of sensors that can be embedded in the system while causing mechanical reliability issues.

Here, this work presents a fully portable and highly skin-conformable at-home sleep monitoring system that integrates soft and functional materials with electronics for a comfortable yet reliable wearable system. This wireless wearable platform addresses the

[1]IEN Center for Human-Centric Interfaces and Engineering at the Institute for Electronics and Nanotechnology, Georgia Institute of Technology, Atlanta, GA 30332, USA. [2]George W. Woodruff School of Mechanical Engineering, Georgia Institute of Technology, Atlanta, GA 30332, USA. [3]School of Electrical and Computer Engineering, Georgia Institute of Technology, Atlanta, GA 30332, USA. [4]Department of Radiology, Icahn School of Medicine at Mount Sinai, BioMedical Engineering and Imaging Institute, New York, NY 10029, USA. [5]Metal Powder Department, Korea Institute of Materials Science, Changwon 51508, Republic of Korea. [6]School of Electrical Engineering, Korea Advanced Institute of Science and Technology, Daejeon 34141, Republic of Korea. [7]Emory Sleep Center and Department of Neurology, Emory University School of Medicine, Atlanta, GA 30329, USA. [8]Department of Psychology, University of Texas at Austin, Austin, TX 78712, USA. [9]Wallace H. Coulter Department of Biomedical Engineering, Georgia Tech and Emory University, Atlanta, GA 30332, USA. [10]Parker H. Petit Institute for Bioengineering and Biosciences, Institute for Materials, Neural Engineering Center, Institute for Robotics and Intelligent Machines, Georgia Institute of Technology, Atlanta, GA 30332, USA.
*Corresponding author. Email: whyeo@gatech.edu
†These authors contributed equally to this work.

Downloaded from https://www.science.org on September 01, 2025

existing challenges and limitations of the gold-standard sleep monitoring tools and methods used at sleep clinics. This paper describes the unique advantages of soft hybrid manufacturing and packaging technologies to offer enhanced mechanical reliability and comfortable wearability with conformal device lamination to the skin. Laser micromachining shows scalable manufacturing of nanomembrane stretchable sensors and interconnectors. A composite of elastic fabric and ultrasoft silicone elastomer makes a substrate to integrate sensors and electronics together, providing strain distribution and strong adhesion to the skin. The soft wearable platform, mounted on the face, wirelessly measures high-quality sleep physiological signals, including EEG, EOG, and EMG, which are comparable to the data recorded by the PSG system at a sleep clinic. In addition, we develop a deep-learning algorithm, convolutional neural networks (CNNs). When the CNN is embedded in the portable sleep patches, we are able to get automated quantitative sleep scoring and apnea detection. A clinical study involving sleep patients and healthy controls fully validated the wearable device's performance. This portable platform only needs two unobtrusive patches for clinical-grade sleep analysis that use Bluetooth to deliver data to a tablet or smartphone wirelessly. Unlike the PSG, requiring more than 10 wired sensors and bulky electronics, the developed wearable patch can be used anywhere, such as at a user's home, offering a natural and comfortable sleep. Collectively, the wireless wearable biomedical systems that combine machine learning technologies show a great potential to expand home-sleep monitoring opportunities while capturing other application opportunities in home health care, digital health monitoring, and quantitative disease diagnosis.

## RESULTS

### Design, structures, and fabrication of at-home sleep monitoring patches

Figure 1A presents an overview of an at-home sleep monitoring patch. The portable wearable sleep monitor includes two small patches: one for measuring EEG and EOG on the forehead and the other for measuring EMG on the chin. These physiological signals are analyzed in real time to detect sleep stages and disorders. The soft and unobtrusive patch has an exceptionally smaller form factor than other wearable sleep monitors (Fig. 1, B and C), offering seamless integration with the skin for high-fidelity, reliable signal detection during sleep. All measured data are wirelessly transmitted via Bluetooth to a mobile device such as a smartphone or a tablet. The data are then analyzed with CNN in real time for automated sleep scoring and apnea event detection. Photos in Fig. 1 (B and C) highlight the wearable patch's intimate contact with the face, specifically the forehead and chin. Figure 1D shows the front side of the highly soft membrane patch on a polytetrafluoroethylene (PTFE) substrate for easy handling. Photos in Fig. 1 (E and F) show the device's back side incorporating skin-contact nanomembrane electrodes that are highly stretchable and flexible. Collectively, the soft wearable platform provides user comfort, ease of use, and portability, such that users can easily follow instructions to measure their sleep at home without technicians. An example in movie S1 shows a device manual that users can easily follow compared to a complicated, time-consuming PSG setup. Illustrations in Fig. 1 (G and H) capture the details of integrated sensors and electronics in the wearable system. All electronic components are embedded in a soft fabric composite made of elastic nonwoven polyurethane and medical-grade silicone adhesive (Silbione, Elkem). The fabric packaging provides a nonsticky dry surface for convenient device handling while protecting the electronics from excessive mechanical deformation (*26*, *27*). In addition, the inner layer of a silicone adhesive incorporates nanomembrane electrodes and stretchable copper interconnectors, facilitating enhanced skin contact. The dry electrodes on a patterned polyimide film offer reusability for multiple days of sleep recording, unlike the one-time-use gel electrodes in the gold-standard PSG (*28*–*30*). The electrode and the integrated circuit relate to a stretchable copper interconnector encapsulated with an elastomer. On the fabric side of the device, the multilayered flexible circuit includes a Bluetooth-based wireless module and a rechargeable Li-polymer battery. This patch uses a 150-mAh Li-polymer battery for the forehead unit, and the power consumption is 52.61 mW with a battery life of 10.55 hours. The chin patch uses a 110-mAh Li-polymer battery, and the power consumption is 34.06 mW with a battery life of 11.95 hours. A clip in movie S2 captures an example of how the wearable system can wirelessly measure EEG, EOG, and chin EMG signals using a table. Table 1 summarizes and compares our work with other EEG-based wearable sleep monitors, capturing the unique advantages of the soft wearable sleep patch. Our wireless system that measures multiple physiological signals offers a clinical assessment of sleep quality and disorder with multiple patients, showing the highest accuracy to date. Specifically, its highest sleep scoring agreement with PSG, in both manual and automated analysis, captures a clear advantage using our CNN-based classification model.

Figure 2 presents the details of the wearable system's architecture and fabrication procedures. We carefully chose the targeted locations of electrodes for measuring EEG, EOG, and chin EMG by following the PSG setup and the standards from AASM (Fig. 2A) (*31*). As a result, there are two-channel EEG electrodes (EEG1 and EEG2), two-channel EOG electrodes (EOG1 and EOG2), and a single-channel chin EMG electrode with their ground and reference electrodes. A diagram in Fig. 2B shows the overall flow of how we measure and analyze data. This system includes a multichannel differential amplifier and Bluetooth low-energy microcontroller with a 2.4-GHz antenna. A table or phone, embedding the CNN algorithm, processes and analyzes the recorded data to provide sleep stage classification and apnea detection outputs. For the fabrication of multiple devices, we developed a scalable manufacturing method using laser micromachining of stretchable electrodes and interconnectors. The femtosecond laser process offers high-precision processing of various materials and high-throughput manufacturing of complex structures (*23*). Photos in Fig. 2 (C and D) show a fabricated array of gold electrodes on a 5-inch square plate and a corresponding microscopic image of the electrode with curved patterns, providing enhanced stretchability and mechanical reliability (*23*, *24*, *32*). The laser spot size used in this fabrication is 13 μm, and the pattern width of each electrode is 124 μm, providing enough skin contact. Photos in Fig. 2 (E and F) show a set of fabricated copper interconnectors on a large glass (8 inches by 10 inches), which makes an electrical connection between multiple electrodes and integrated circuits. In this work, we used copper connectors to offer enhanced solderability and robust electrical connections with the device (Fig. 2F). The connector's pattern width is 79 μm, and the laser spot size is 18 μm. The laser spot size is larger than the electrode case because higher laser power and repetition are required due to copper's higher thermal conductivity and thickness.

Downloaded from https://www.science.org on September 01, 2025

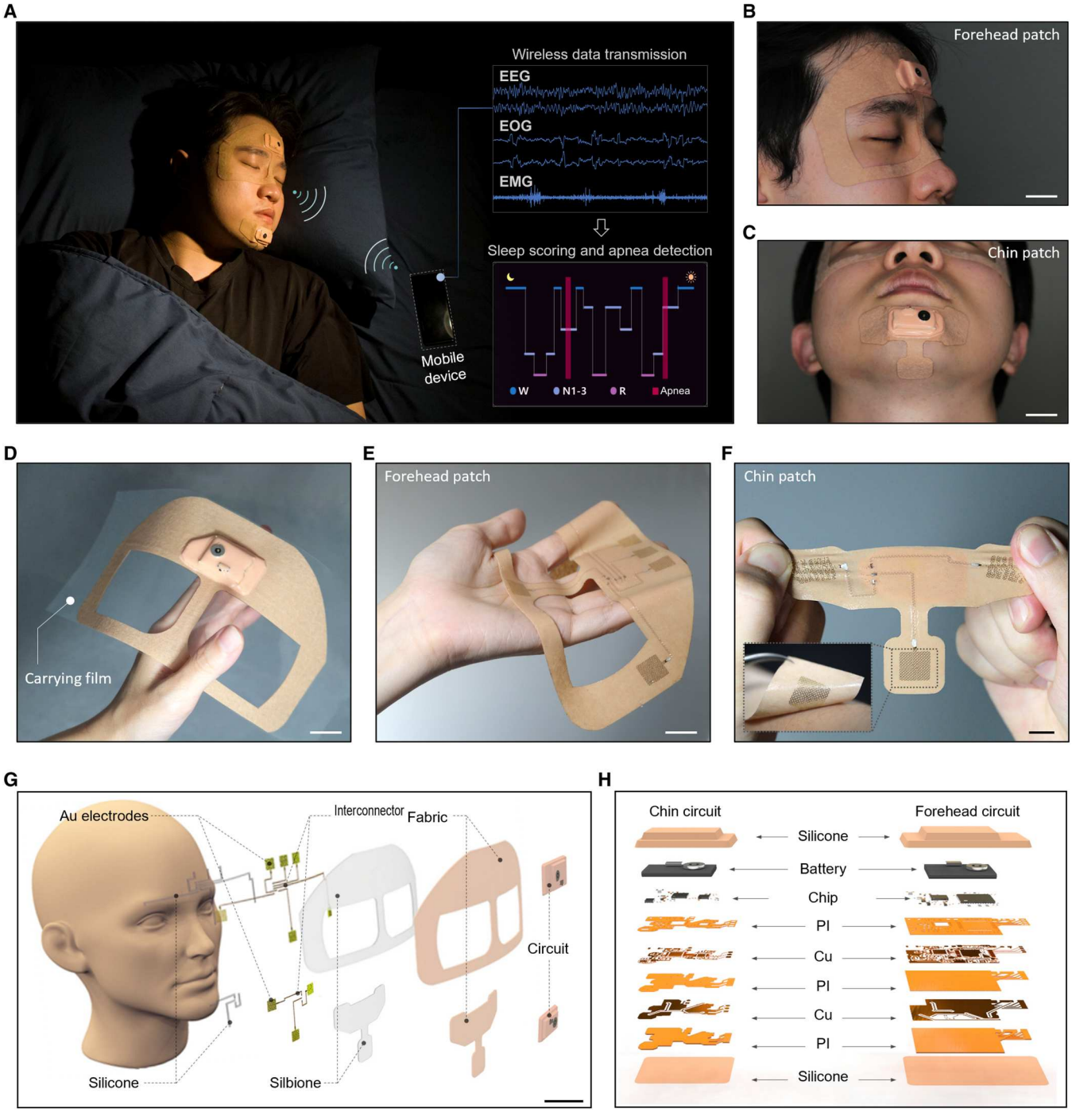


**Fig. 1. At-home sleep monitoring patches for assessing sleep quality and sleep apnea.** (**A**) Image of an at-home wireless sleep monitoring system for real-time, multichannel recording of EEG, EOG, and EMG signals and deep learning–based classification of sleep stages and sleep apnea detection using a portable device. (**B** and **C**) Photos of the soft wearable patches conformally attached to the facial area, including the forehead (B) and the chin (C). Scale bars, 2 cm. (**D**) Photo of the forehead patch on a device carrier made of PTFE for convenient handling and storage for multiday uses. Scale bar, 2 cm. (**E**) Photo of the backside of the highly flexible soft patch in (D) showing nanomembrane electrodes. Scale bar, 2 cm. (**F**) Photo of the chin patch showing its stretchability to make conformal lamination to the skin (inset image). Scale bar, 1 cm. (**G**) Illustration of the sleep monitoring system mounted on the face, including electrodes, interconnectors, circuits, and adhesive (Silbione) on a fabric. Scale bar, 3 cm. (**H**) Details of the multilayered flexible circuits, made of metals, polymers, and chips, which are fully encapsulated by silicone membranes for strain isolation during device assembly, handling, and wearing during sleep.

Downloaded from https://www.science.org on September 01, 2025

**Table 1. Comparison of EEG-recording wearable sleep monitors.**

| Reference | Form factor | Electrode type | Detecting signals* | | | Clinical validation with patients (number) | Manual scoring accuracy (%/kappa†) | Automated scoring accuracy (%/kappa) | Disorder detection accuracy (%) |
|---|---|---|---|---|---|---|---|---|---|
| | | | EEG | EOG | EMG | | | | |
| This work | Soft, wireless patch | Stretchable, conformable nanomembrane (dry) | O | O | O | Yes (8) | 82.43/0.74 | 83.89/0.76 | 88.52‡ |
| (*12*) | Rigid, wired headband | Conventional gel (wet) | O | O | O | – | – | 74/– | – |
| (*13*) | Flexible, wired patch | Printed composite (dry) | O | O | O | – | – | – | – |
| (*14*) | Rigid, wired headband | Dry conductive foam and conventional (wet) | O | X | X | – | – | 76.7/0.69 | – |
| (*15*) | Rigid, wireless headband | Conventional gel (wet) | O | O | X | Yes (40) | – | 71.3/0.63 | – |
| (*16*) | Rigid, wireless headband | Rigid flat metal (dry) | O | X | X | – | – | 83.5/0.75 | – |
| (*17*) | Wired ear plug | Conductive fabric (dry) | O | X | X | – | – | 74.1/0.61 | – |
| (*18*) | Wired ear plug | Rigid iridium oxide (dry) | O | X | X | – | – | 80.5/0.73 | – |
| (*19*) | Wired patch | Printed Ag with conductive gels (wet) | O | X | X | – | 55/0.38 | 70/0.58 | – |

*EEG, electroencephalograms; EOG, electrooculograms; EMG: electromyograms. †Cohen's kappa value. ‡Only data showing sleep disorder detection in patients.

Overall, the laser micromachining of electrodes and interconnectors enables fast, reliable, and scalable manufacturing capabilities. An example in movie S3 shows how we used a laser to fabricate the critical components of the wearable system. The electrode, connected with the stretchable wire via soldering, maintains mechanical stability when mounted on a soft fabric (Fig. 2G). In contrast to the conventional woven fabric, the advantage of the fabric composite is its omnidirectional elasticity (Fig. 2H) and convenient processibility without untangling due to its nonwoven structure composed of a random network of fibers. Another advantage is that the soft silicone adhesive (Silbione) penetrates through the networks of fabric fibers to achieve mechanical interlocking for robust integration of the bilayer while leaving the top side of the fabric dry and nonsticky for handling (Fig. 2, I and J). This soft packaging method using the fabric provides strain isolation (fig. S1) to avoid mechanical damage to the electronics during device assembly, handling, and multiple uses during sleep (*33*–*35*). The additional details of device fabrication appear in fig. S2 and Methods. In addition, the details of the wireless circuit that we developed appear in fig. S3, which shows two devices mounted on the forehead and the chin.

## Mechanical and material characterization of the soft wearable system

This study captures the mechanical properties of the developed soft electrodes and interconnectors via computational modeling and experimental validation. The finite element analysis (FEA) results in Fig. 3 (A and B) capture the mechanical stretchability of the designed structures up to 30%, showing that maximum strains on the gold and copper membranes remain well below fracture and yield strains (1 and 0.3%, respectively) (*36*, *37*). Additional FEA study shows that the electrode and connector can stretch up to 108 and 110% before fracture and yield, respectively (fig. S4). The maximum tensile strain the structure can endure is above 200% before fractures (fig. S5). An experimental study in Fig. 3C validates the mechanical reliability of fabricated components during a stretching test. The testing coupons include Au electrodes and Cu connectors to facilitate more accurate stretching measurements (inset image of Fig. 3C). There are no observed fractures or yielding features. Cyclic stretching of the electrode and connector and electrical measurements in Fig. 3D proves the safety for multiple uses. With 1000 cycles of 30% tensile stretching, there is negligible change in resistance with intermittent artifacts. Experimental validation of the omnidirectional stretchability and elasticity of the fabric shows the fabric's stretchability above 300% with Young's modulus of 1.29 MPa and Poisson's ratio of 0.184 (fig. S6). In addition, we conducted additional sets of experiments to find the optimal material's thickness and peeling strength by using the soft silicone adhesive (Silbione). As summarized in Fig. 3E, the membrane's thickness decreases according to the coating speed of the material on a substrate (details of experimental conditions in fig. S7). On the other hand, the peeling strength is proportional to the thickness due to the increased energy required for the elastomer's deformation. In

Downloaded from https://www.science.org on September 01, 2025

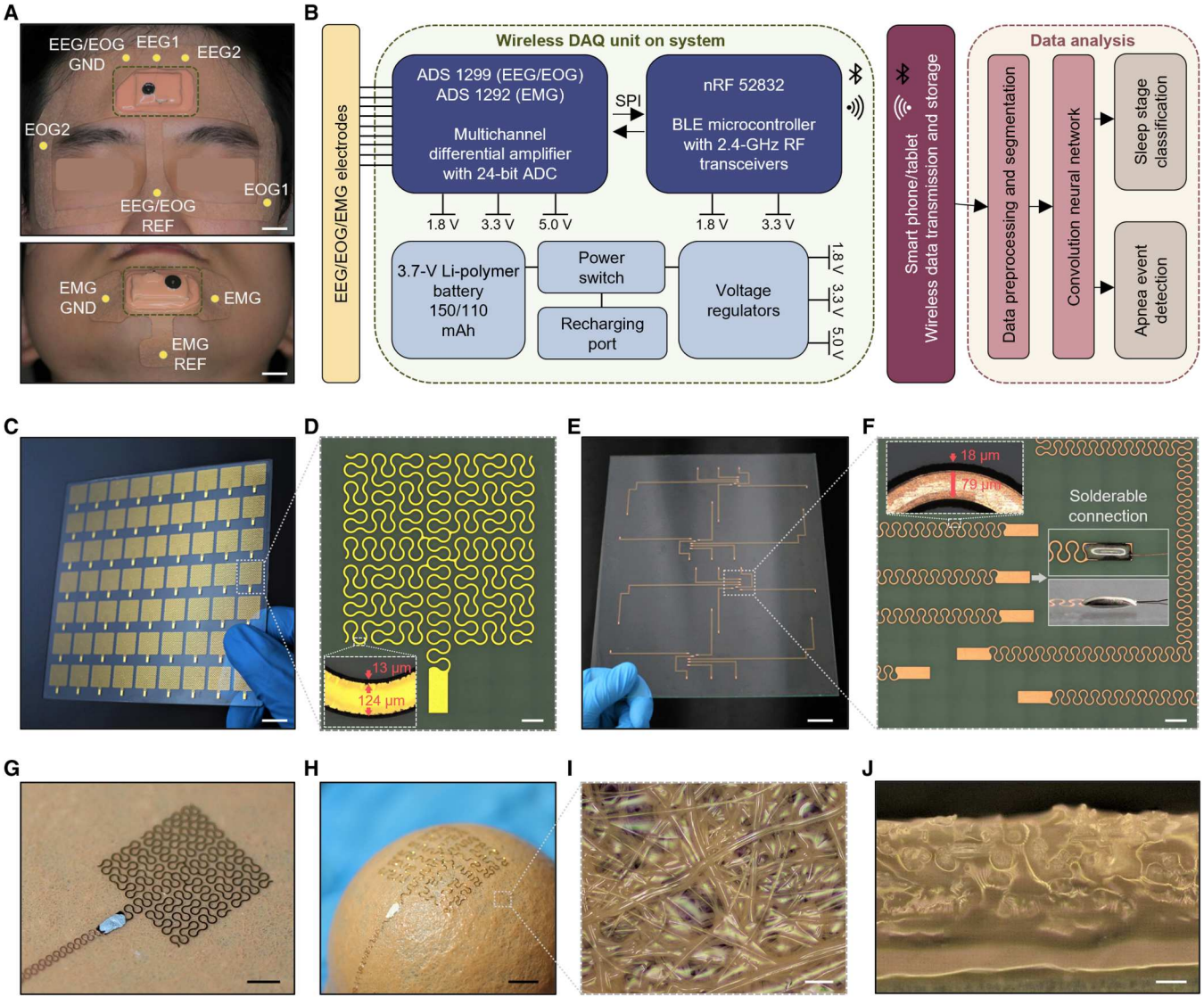


**Fig. 2. System architecture and fabrication of sleep monitoring devices.** (**A**) Specific locations of electrodes in the sleep patches for monitoring EEG, EOG, and EMG. Scale bar, 1 cm. (**B**) Diagram showing the sequence from physiological signal detection to Bluetooth (BLE) based wireless data transmission and processing with a deep learning algorithm. DAQ, data acquisition. ADC, analog to digital converter. SPI, serial peripheral interface. RF, radiofrequency. (**C**) Photo of a 7 × 9 array of nanomembrane electrodes fabricated via laser micromachining on a 5-inch glass capturing its scalable manufacturability. Scale bar, 1 cm. (**D**) Optical microscope image of an electrode in (C), showing open-mesh patterns. Scale bar, 1 mm. (**E**) Photo of four sets of stretchable copper interconnectors fabricated via laser micromachining on an 8 inch–by–10 inch glass. Scale bar, 2 cm. (**F**) Optical microscope image of interconnectors with the solderable contact pad for connecting electrodes and circuits. Scale bar, 1 mm. (**G**) Fabricated electrode integrated with a piece of soft fabric after transfer printing and connecting with a stretchable interconnector. (**H**) Demonstrated stretchability of the electrode in (G) by conformally wrapping around a 1-inch-diameter sphere. (**I** and **J**) Optical microscope images of a fabric-silicone adhesive composite enclosing the electrode, showing a top-view structure (I) and a cross-sectional view (J). The soft silicone adhesive penetrates through the networks of fabric fibers to achieve mechanical interlocking for robust integration of the bilayer. Scale bars, 3 mm.

this study, we determined that a 250-μm-thick membrane is ideal for providing enough peeling strength and skin conformability. A graph in Fig. 3F summarizes measured peeling strength values and signal-to-noise ratio (SNR) of measured contact signals with the skin for 7 days of sleep. This result shows high degradation of peeling strength when the device is not washed, whereas the soap-washed specimen shows marginally degraded peeling strength. The major degradation factors in adhesion are dirt and skin oil that can be washed off by cleaning with soap (*26*). The SNR values with washed devices show minimal changes in SNR throughout 7 days of monitoring, offering a multinight use of the wearable patch for detecting high-fidelity sleep data at home. When measuring physiological sleep signals, the wearable device's skin contact quality is critical to maintaining low skin-dry electrode contact impedance (*28*, *30*, *38*). Therefore, we developed a model for quantitative analysis by assuming that a wearable patch has enough deformability and stretchability to fill the gap between the skin's sinusoidal morphology and the backing layer's flat surface (detailed description in

Downloaded from https://www.science.org on September 01, 2025

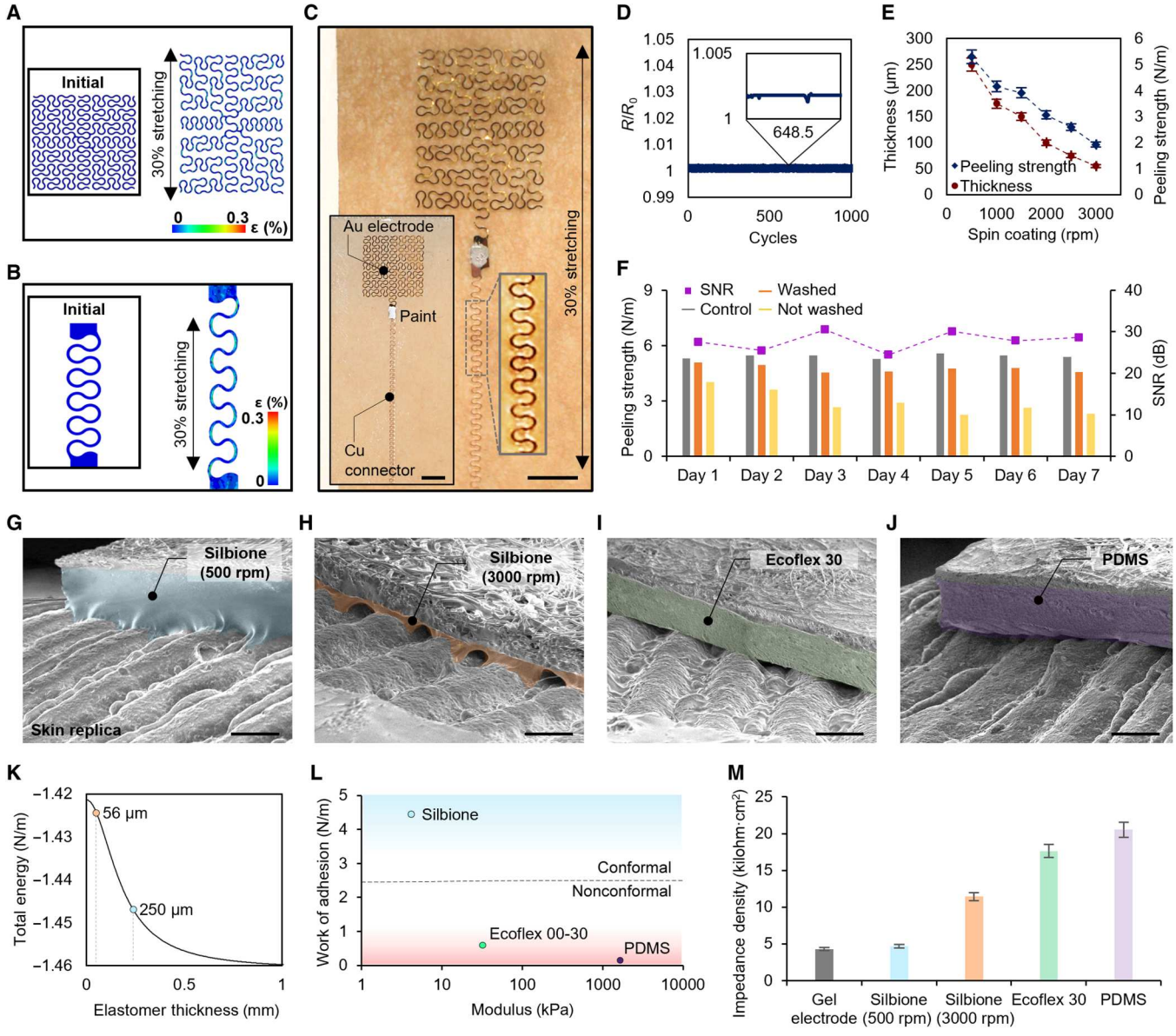


**Fig. 3. Mechanical and material characterization of the wearable system.** Computational modeling results predicting mechanical stretchability (30%) of an Au electrode (**A**) and a Cu interconnector (**B**). (**C**) Photo of an electrode connected with an interconnector under stretching up to 30%, showing no adverse outcomes. Scale bar, 500 μm. (**D**) Change in electrical resistance of the integrated electrode in (C) throughout a cyclic stretching test (1000 cycles with 30% strain), demonstrating its reliability with a negligible change in relative resistance. (**E**) Change of a silicone adhesive (Silbione) in thickness and peeling strength according to its spin-coating speed (revolutions per minute). (**F**) Peeling strength and signal-to-noise ratio (SNR) values of a skin-mounted electrode during 7 days. Among them, a sample that is cleaned with soap daily maintains the skin-contact quality and mechanical reliability throughout the 7 days, such as the control sample. (**G** to **J**) SEM images of four substrates on a skin replica showing the quality of surface contact. Samples are made of different materials, including two silicone adhesive layers: spin-coated at 500 rpm (G) and spin-coated at 3000 rpm (H), Ecoflex 30 (I), and PDMS (J). Scale bars, 300 μm. Colorized areas show the coated soft materials on a fabric. (**K**) Plot of theoretical total interfacial energy depending on an elastomer thickness (Silbione). (**L**) Conformal contact analysis determined by work of adhesion and Young's modulus. The dashed line represents the critical points deciding conformal or nonconformal regimes. (**M**) Impedance density measurements from various substrate compositions in (G) to (J), showing that the thin silicone adhesive layer in (G) offers conformal contact of a fabric-embedded electrode with the human skin. The contact quality of the dry substrate is similar to a conventional electrode with conductive gels.

Downloaded from https://www.science.org on September 01, 2025

note S1). The skin conformal contact can be determined by this equation showing the interactions with the skin

$$U_{\text{conformal}} = U_{\text{bending}} + U_{\text{silicone}} + U_{\text{skin}} + U_{\text{adhesion}}$$

In this model, there are three key properties of a patch regarding the elastomeric membrane's thickness work of adhesion and Young's modulus. Our experimental study validates the analytical study as summarized in Fig. 3 (G to M). Scanning electron microscopy (SEM) images in Fig. 3 (G to J) show examples of skin-electrode contact quality, depending on the membrane material and thickness. Among these cases, a soft membrane layer made of Silbione (500 rpm; thickness: 250 μm; Fig. 3G) offers the best contact quality, which is more advantageous than the one in Fig. 3H (thickness: 56 μm) due to less amount of strain required for conformal deformation. A graph in Fig. 3K shows an analytical calculation of total interface energy with varying thicknesses of Silbione, where more negative energy from thicker membranes indicates higher conformability. On the other hand, two other examples of Ecoflex 30 and poly(dimethylsiloxane) (PDMS) have poor contact quality due to the high Young's modulus and low work of adhesion. A diagram in Fig. 3L summarizes the analytical study outcomes of this study, showing the relationship between work of adhesion, modulus, and resultant conformal skin contact. Figure S8 shows the details of the experimental setup and measured values of the work of adhesion for each membrane. Last, we measured skin-electrode contact impedance data to compare the performance of the wearable patches with different membrane substrates with the standard Ag/AgCl wet electrode. As summarized in Fig. 3M, the soft adhesive membrane in Fig. 3G shows the best skin-contact quality, such as the gel electrode.

## Clinical study outcomes of sleep quality via comparison with the gold-standard PSG

This study demonstrates the fabricated wearable sleep device's performance via side-to-side comparison with the gold-standard PSG setup. A photo in Fig. 4A shows a participant in a sleep clinic wearing two different systems; there are two unobtrusive wearable patches on the forehead and chin, but the PSG setup requires more than 15 wired bulky sensors and a separate data acquisition system. The physiological signals in Fig. 4B, measured during sleep, compares the data quality in detecting five sleep stages [awake, N1, N2, N3, and rapid eye movement (REM)]. Each of the five sleep stages is distinguished by its characteristic signals from measured EEG, EOG, and EMG. The signal features are either continuous waves (alpha, theta, delta, and EMG baseline) or instantaneous signals (sleep spindle, K-complex, and REM), showing different amplitudes, frequencies, morphologies, and durations. Sleep fragmentation in EEG and EOG channels is often observed during apnea events, which is characterized by a series of temporary suppression of power in the lower frequency range and bursts of power in the middle to high-frequency range. PSG and wearable patch data come from locations of F3-M2 channel and EEG1 channel, respectively. The visualization and morphology analysis of these signals is critical because the standard sleep analysis uses this method (*31*). Overall, the characteristic signal morphology from the wearable patch shows high similarity to that from PSG, and the patch's data can distinguish each sleep/wake stage. The average SNR value of our system (22.77 dB) is comparable to that of PSG (25.52 dB). The lower signal amplitude comes from the patch's reference location on the nose, which is an acceptable alternative place (*39*). Raw sleep data measured by the wearable patch is shown in fig. S9 with all five channels during five sleep stages. Additional analysis in Fig. 4 (C and D) compares spectrogram sleep data, showing similar spectral profiles throughout the sleep. The spectral power comparison over the four main EEG frequency bands (delta, theta, alpha, and sigma) shows high correspondence with the Pearson correlation value of 0.76 and $P$ value of less than $10^{-10}$. Details of the power values appear in fig. S10. The signal quality was further validated by scoring the sleep data from both systems. A sleep technician conducted this scoring with blind datasets to avoid bias.

Summarized results in Fig. 4 (E and F) present two representative examples of the manual scoring analysis, which shows strong agreement (87.50 and 88.19%) with a high Cohen's kappa (κ) value (0.80 and 0.82) between the two systems. The confusion matrix in Fig. 4G summarizes the comparison results acquired from eight subjects detecting five sleep stages. The overall accuracy is 82.43% with Cohen's kappa value of 0.74, which is very close to the reported average interscorer reliability value of 82.0% with Cohen's kappa value of 0.76 (*40*). The wearable patch shows the highest performance in scoring accuracy among wearable EEG monitors (details in Table 1). The accuracy is calculated by following this equation: Accuracy = (true positive + true negative)/(true positive + false positive + true negative + false negative).

The sparse occurrence of N1 sleep stage and the ease of confusion between W-N1 and N1-N2 transitions are key reasons for its low agreement rate despite being generally well known with the lowest scoring accuracy in both manual and digital analysis. Cohen's kappa coefficient for stage N1 is 0.23, which is not much different from the reported values of 0.24 (*41*). Integration of planar electrodes with soft materials has been widely adopted in multiple studies for prolonged data acquisition, even under vigorous motion or activity (*24*, *34*, *35*, *42*). An example of data in fig. S11 presents 7-day-long sleep results measured at home, demonstrating the consistent data quality maintained throughout the prolonged measurements. Overall, this study validates that the wearable patch can measure physiological sleep data at the level of clinical standards. Compared to the standard PSG system, our wearable patch has unique advantages of portability, accessibility, and multiday use. This device can be readily usable at home for detecting sleep data for a week.

## Measurements of sleep stages and detection of sleep apnea from controls and patients

Figure 5A shows an EEG hypnogram and a spectrogram measured from a healthy control using the wireless wearable patch. As clearly categorized in the hypnogram, this subject shows stable and uniform cycles of sleep stages without the indication of apnea. In this analysis, we also used the multitaper spectrogram analysis for quantifying various features of EEG and EOG in both time and frequency domains, providing a more accurate analysis than the traditional single-taper spectrogram (*43*). A representative example in fig. S12 shows how we used the multitaper method to analyze sleep data. A set of data in Fig. 5B shows a close-up view of spectrograms and EEG and EOG that capture the progression from the awake stage (W) to non-REM (N3) stage with corresponding characteristic signal features. During stage W, eyes are closed, showing

Downloaded from https://www.science.org on September 01, 2025

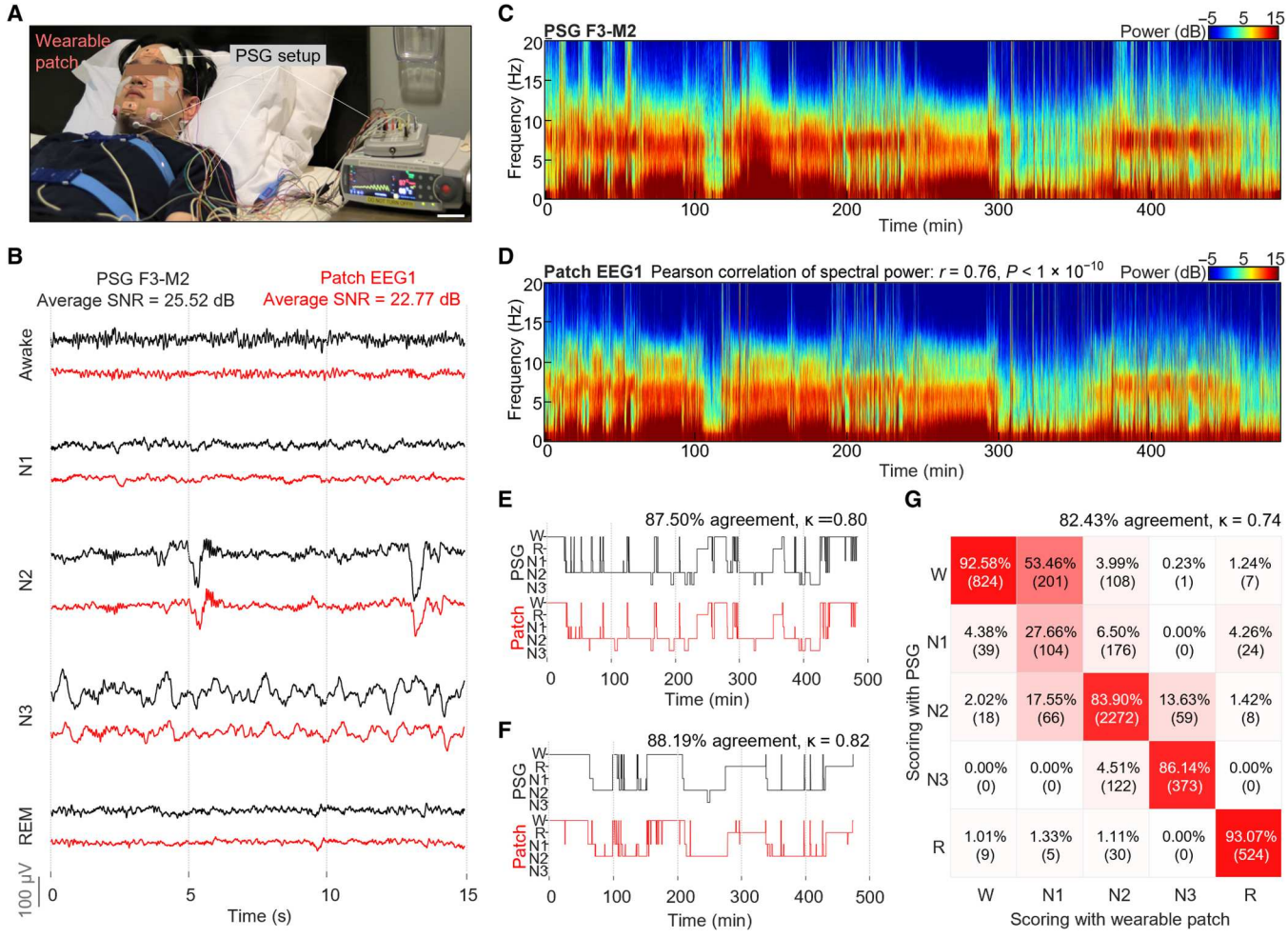


**Fig. 4. Clinical study outcomes of sleep quality via comparison with the gold-standard PSG.** (**A**) Comparison of two different setups for sleep monitoring. The wireless sleep patches show unobtrusive integration with the face, while the gold-standard PSG setup requires many wired sensors, external connectors, and bulky electronic systems. Scale bar, 6 cm. (**B**) Side-to-side comparison of raw EEG data measured from both the PSG system (F3-M2 channel) and the forehead patch (EEG 1), capturing each of the five sleep stages (awake, N1, N2, N3, and REM). The wearable patch's data are very similar to the one from the PSG. Comparison of spectrograms from (**C**) the PSG (F3-M2 channel) and (**D**) the sleep patch (EEG 1 channel of forehead) simultaneously measured from the same subject. Hypnograms that compare sleep data and manual scores were evaluated by a sleep specialist. In the comparison, black and red curves show the data from the PSG device and the wearable device, respectively, for two subjects—one in (**E**) and the other in (**F**). (**G**) Confusion matrix showing a high agreement (82.43% and kappa value = 0.74) between two devices. This comparison uses sleep data and manual scoring results from eight subjects who wear two devices simultaneously during sleep.

10-Hz alpha waves as indicated in the EEG spectrogram. During N1, low-amplitude mixed-frequency (LAMF) signals are observed, and its spectrogram shows weaker spectral power than other stages. During N2, the EEG spectrogram captures the increase in low-frequency delta wave activity, with frequent occurrence of microevents such as K-complex, delta waves, and sleep spindle. During N3, the EEG spectrogram depicts the continuous and uniform activity of strong low-frequency delta (slow wave). Comparison of spectrograms of EOG and EEG further facilitates distinguishing sleep stages. During stage N1, the spectrogram of EOG shows strong activity in the lower frequency that corresponds to slow eye movement. Besides N1, EOG spectrogram shows a mirror image of the EEG spectrogram with weaker spectral power. Additional datasets in Fig. 5C present other features. During stage R, the EEG spectrogram shows LAMF, similarly with N1, while EOG spectrogram captures strong and irregular activity in the lower frequency that corresponds to REM. In contrast to the healthy participant, a patient with severe sleep apnea shows completely different, highly fragmented sleep cycles with frequent arousals (Fig. 5D) due to apnea events, causing the deteriorated quality of sleep and tiredness. The hypnogram in Fig. 5E captures the numerous arousals following a series of apnea, and the corresponding spectrogram is highly fragmented and dominated by alpha waves around the arousal events. Spectrogram data in Fig. 5F further depicts the characteristics of fragmented sleep signals. At the onset of each apnea event, the low-frequency spectral power typical of non-REM sleep becomes suppressed. A burst of spectral power throughout a wide range of frequencies, from delta to sigma, occurs after the apnea event. Overall, this study shows the capability of our data analysis to distinguish the difference between healthy sleep and apnea.

Downloaded from https://www.science.org on September 01, 2025

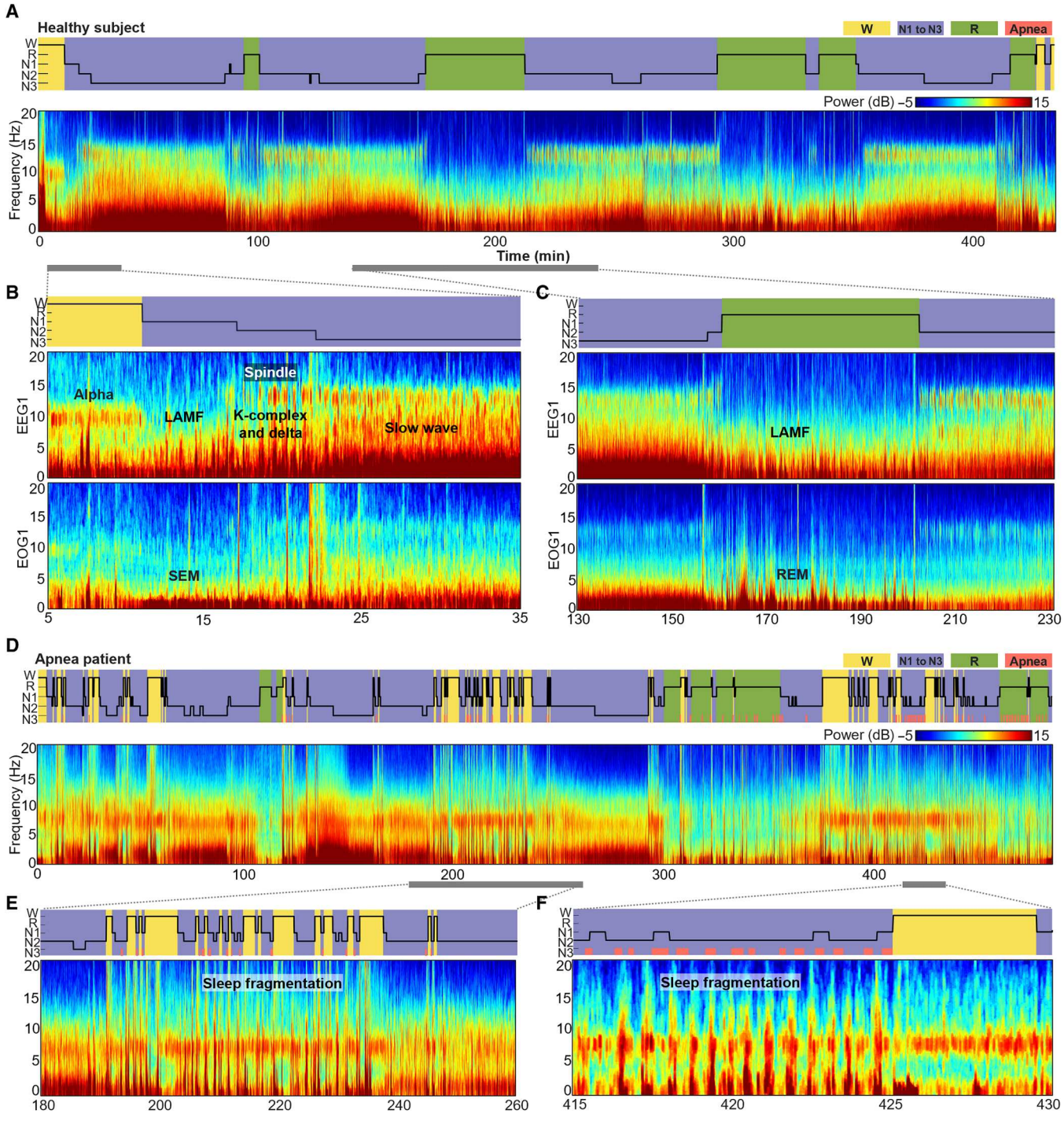


**Fig. 5. Measurements of sleep stages and detection of sleep apnea from patients.** (**A**) Hypnogram and spectrogram of a healthy subject showing a gradual change in sleep/wake stages without much abrupt fluctuation throughout the sleep. (**B** and **C**) Detailed data showing hypnogram, EEG, and EOG spectrograms from the yellow and green highlighted region in (A). The exploded views capture characteristic signals of each sleep/awake stage, including alpha, slow eye movement, REM, slow wave, and more. (**D**) Hypnogram and spectrogram measured from a sleep apnea patient showing a frequency fluctuation and fragmentation of sleep throughout the sleep. (**E** and **F**) Close-up view of the serial apnea events and frequent arousals with corresponding hypnogram and spectrogram. These detailed data show abrupt awakening after a series of apnea events and characteristic signals of sleep fragmentation follow suiting each apnea event.

Downloaded from https://www.science.org on September 01, 2025

### Automated sleep scoring and quantitative diagnosis of sleep apnea using CNN

As discussed earlier, the standard method in sleep analysis is to use visual data observation and manual scoring by technicians, causing delays, additional costs, and human errors (*5*, *44*, *45*). Thus, we developed an automated sleep classification and scoring methods using deep learning CNN in this work. Figure 6A depicts a flow from data acquisition to training, processing, and prediction. The illustration in Fig. 6B shows the deep learning architecture developed in this work that uses sleep data measured by the wearable patch for automated sleep scoring. Details of the CNN algorithm, data processing, and classification processes for sleep stage detection and sleep apnea detection appear in figs. S13 and S14, tables S1 and S2, and Methods. Graphs in Fig. 6 (C and D) show two representative results of the automated sleep scoring. When the automated scoring data from the wearable patch is compared to that

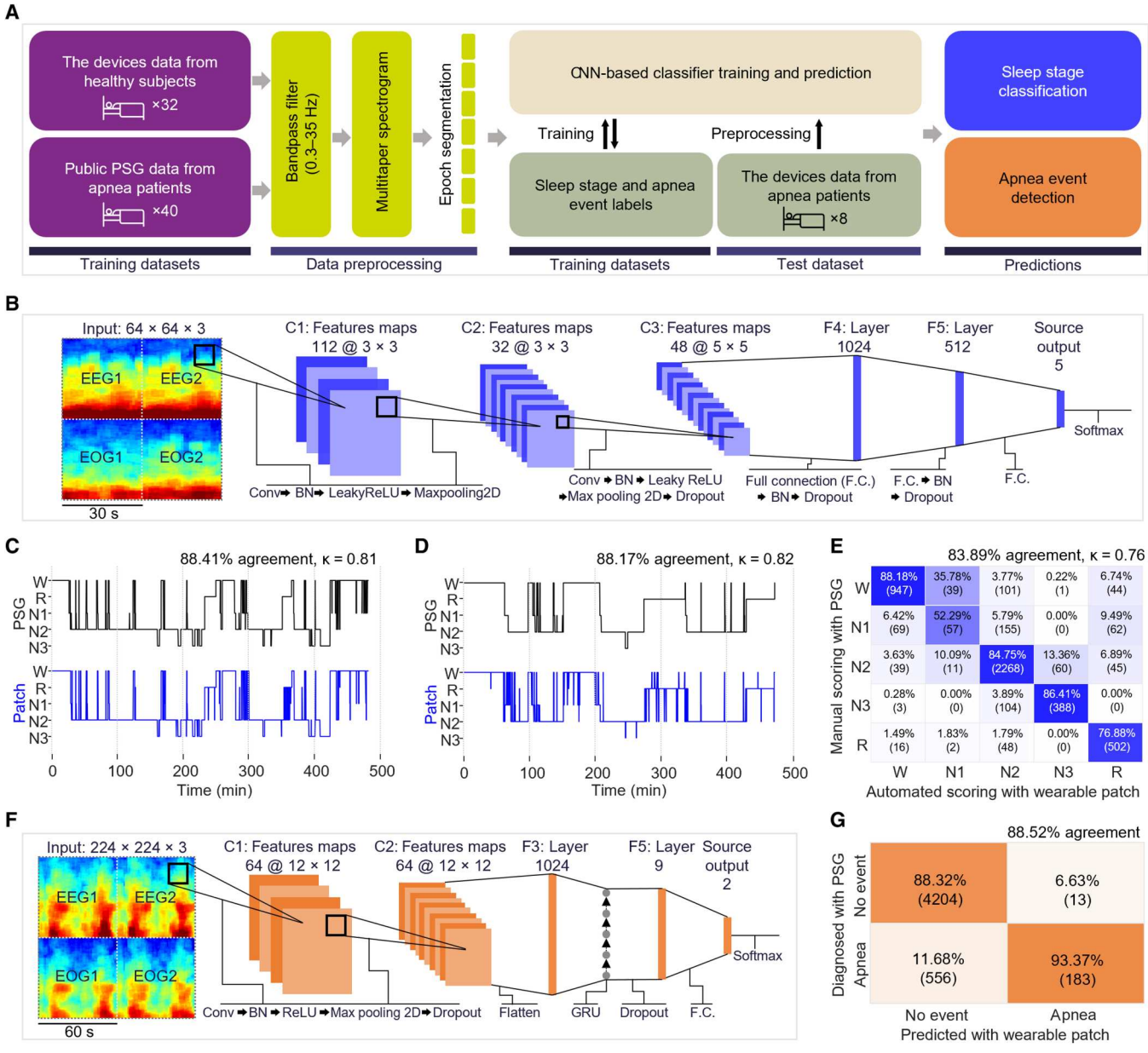


**Fig. 6. Automated sleep scoring and quantitative diagnosis of sleep apnea using CNN.** (**A**) Flow chart illustration for an overview of the data processing and machine learning implementation for sleep scoring and apnea event detection. (**B**) Input data structure and machine learning architectures for automated sleep stage scoring (Conv, convolution; F.C., fully connected layers; BN, batch normalization). (**C** and **D**) Hypnograms comparing manual scorings done by a sleep technologist with the PSG signals (black) and CNN-based automated sleep scoring done with the devices' signals (blue) over two subjects' sleep measurements. (**E**) Confusion matrix showing high agreement between the manual scorings done by a sleep technologist with PSG signals and automated sleep scoring with the devices' signals over all the eight subjects' sleep measurements. (**F**) Input data structure and proposed machine learning architectures for apnea event detection (GRU, gated recurrent unit). (**G**) Confusion matrix showing high accuracy of apnea event detection with our system in comparison with the manual diagnosis by a sleep technologist with PSG.

Downloaded from https://www.science.org on September 01, 2025

from the PSG scoring case, there is strong agreement between the two methods, with an accuracy of 88.41 and 88.17% and Cohen's kappa values of 0.81 and 0.82. The correlation outcomes of sleep scoring have similar results to the manual scoring datasets from Fig. 4. The confusion matrix in Fig. 6E summarizes the performance of our CNN algorithm compared to manual scoring with PSG. The overall agreement and Cohen's kappa between the automated and manual scoring (83.89% and 0.76) showed a better performance than the reported average interscorer reliability (82.0%) (*40*). A set of diagrams in Fig. 6F depicts the input data and the CNN architecture for sleep apnea detection. In the analysis of the confusion matrix (Fig. 6G), our system classified 4760 epochs as no event and 196 epochs as apnea. Among them, a sleep technician diagnosed 4204 epochs as normal and 556 epochs as apnea in the PSG data. Of the 196 epochs, 183 epochs were diagnosed as apnea, while 13 epochs (6.63%) were diagnosed as normal. Thus, with eight patients, the system's performance shows a high accuracy of 88.52%, demonstrating the first study of detecting sleep disorders with the wearable machine learning system. Collectively, this study shows the potential of our system to offer real-time, automated, and accurate detection of sleep stages and disorders, which will advance portable sleep monitoring and home health care.

## DISCUSSION

Collectively, this paper reports the development of a wearable biomedical system that offers at-home wireless sleep monitoring for the clinical assessment of sleep quality and sleep apnea. This work illustrates the first demonstration of automated detection of sleep disorders using a multisensor integrated patch and deep learning algorithm. The wearable platform shows the potential for convenient, reliable, and accurate sleep monitoring and analysis with enhanced accessibility and effectiveness. Our system provides a multimodal physiological measurement with seamless and unobtrusive integration with skin. A combination of materials and fabrication processes enables reliable integration and usability of the system while offering scalable manufacturing of a large-area system. A pilot clinical study compared to standard PSG demonstrates its high signal quality and visual and automated sleep scoring feasibility. Training on existing datasets reflects the device's potential to detect obstructive sleep apnea–related arousals. CNN-based data analysis methods for automated sleep scoring and apnea detection could further validate our system's applicability with high performance. Future studies will focus on improving a wearable electrode's breathability and reusability. Developing a replaceable adhesive layer for the electrode will lower the cost while facilitating long-term use of the wearable sleep monitor. In addition, this system will integrate other sleep sensors for measuring blood oxygen saturation, carbon dioxide, and motions, improving the accuracy and effectiveness of apnea detection. Last, we plan to conduct a large-scale clinical study with patients to validate the efficacy of at-home sleep monitoring and automated disease diagnosis.

## METHODS

### Fabric substrate fabrication

Parts A and B of Silbione (A-4717, Factor II Inc.) were mixed with 1:1 weight ratio for 5 min. To make a uniform thickness of the adhesion layer, mixed uncured Silbione is poured on a PTFE sheet and spin-coated at 500 rpm for 1 min. Brown fabric medical tape (9907T, 3M) was placed on the uncured Silbione surface and followed by a curing process in an oven at 65°C for 30 min. After curing of Silbione, PTFE sheet was detached.

### Nanomembrane electrode fabrication

Gold electrodes were fabricated by electron beam (E-beam) evaporation and facile laser cutting. PDMS (Sylgard 184, Dow) was used for the bottom layer of electrode fabrication because it offers both proper adhesion and easy release feature for this process. A polymer film (18-0.3F, CS Hyde) was laminated on the cured PDMS surface. An E-beam deposition process was used to deposit gold on the film. A precise laser-cutting process was applied to the film to get a stretchable serpentine pattern of the electrode. Last, nonfunctional materials besides the electrode patterns were removed by delaminating from PDMS surface.

### Stretchable connector fabrication

A thin copper foil with a laser cutting process enabled scalable electrical connector fabrication. PDMS was coated and cured on a glass plate (8 inches by 10 inches). A 6-μm-thick copper foil (BR0214, MSE Supplies LLC) was laminated on the cured PDMS surface. A laser-cutting process was applied to the copper foil to get a stretchable serpentine pattern of the electrical connector. Then, the rest of the Cu foil beside the pattern was removed and delaminated from the PDMS surface.

### Fabrication of circuits and encapsulation

Our circuits used a flexible printed circuit board (PCB) board. All electronic components were mounted on the board with a reflow solder process (fig. S3). Tables S4 and S5 contain all the detailed information about the electronic components used in the device. To enhance the mechanical flexibility of the circuit, unnecessary areas were removed with laser cutting. For power supply and management, we used a lithium polymer battery assembly with a slide switch and a circular magnetic recharging port. A low-modulus elastomer (Ecoflex GEL, Smooth-On) is placed underneath the integrated circuit as a strain-isolation layer. The overall electronic system was encapsulated and soft-packaged with an additional elastomer (Ecoflex 00-30, Smooth-On), leaving only the switch and charging port exposed.

### Device assembly

The copper connector and gold electrode were transferred to the soft adhesive side of the fabric with water-soluble tape (ASW-35/R-9, Aquasol Corporation). The localization and alignment of the electrodes can be accurately done with a manual process because of their small size. Once all electrodes are properly placed with the copper connector, the water-soluble tapes on top of all the electrodes are washed off together under flowing water. Silver paint was applied between the copper connector pad and the gold electrode pad. Silver paint offers robust mechanical/electrical connections beyond the yield point of the electrode system. The applied silver paint was dried in an oven at 65°C for 30 min. The copper connector and the silver paint were encapsulated with Ecoflex, which was cured in an oven at 65°C for 180 min. For insulation of the copper connector, elastomer was used rather than polyimide (PI) due to its softer mechanical property and easier manufacturing

Downloaded from https://www.science.org on September 01, 2025

process without the need for a high-temperature process for PI curing, which can cause severe oxidation of copper and thermal damage to the rest of the system. Because of the small area of the Ecoflex-coated region and its surrounding Silbione layers, the Cu interconnector with the Ecoflex encapsulant layer ensures secure contact with the skin, minimizing motion artifacts and maintaining signal quality for the connectors. Electrode system mounted fabric was patterned by laser-cutting process. The soft-packaged electronic system was attached to the fabric side of the fabric substrate by adding and curing a thin silicone layer.

Breathability is one of the important aspects of the wearable system for prolonged skin-interfaced application. We validated this property by measuring a moisture vapor transmission rate among the commonly used silicone elastomers (fig. S15). The measured breathability of the fabric substrate is about two times higher than PDMS with the same thickness and a quarter of the commonly used medical dressing (Tegaderm, 3M Medical). Accumulation of sweat was often observed during our measurements, but it was not critical to the point that it would cause the system′s failure or measurement. In addition, the fabricated soft patch with gold electrodes shows no skin irritation or other side effects. Figure S16 shows comparison test results wearing the soft patches and commercial get electrodes for 3 days.

### Computational modeling

Mechanical deformations and strain distributions associated with the system on human skin were characterized using three-dimensional (3D) FEA. Eight-node 3D solid elements were used to simulate the fabric and Silbione, and four-node shell elements with a two-layer (gold/PI) for the electrode and copper/PI for the connector) were adopted, with optimized meshes to assure computational precision. Displacement-type boundary conditions were assigned to the fabric′s side surfaces where varying amounts of stretching were applied. Elastic stretchability is defined as the point at which the maximum strain in the metal layer exceeds the yield strain (0.30% for copper and 1% for gold) throughout at least half of the width of any segment. The Young′s modulus ($E$) and Poisson′s ratio ($\nu$) of the materials used in the simulations include $E_{au}$ = 78 GPa and $\nu_{au}$ = 0.44 for gold, $E_{pi}$ = 2.5 GPa and $\nu_{pi}$ = 0.34 for polyimide, $E_{cu}$ = 119 GPa and $\nu_{cu}$ = 0.34 for copper, under fabric ($E_f$ = 1.28 MPa, $\nu_f$ = 0.184) with Silbione ($E_{si}$ = 5 kPa, $\nu_{si}$ = 0.48).

### Experimental study of mechanical reliability

For the mechanical characterization of fabric′s elasticity, the fabric (30 mm by 80 mm) was mounted on a motorized testing machine (ESM303, M5-5, Mark-10). The fabric was gently stretched at 50 mm/min up to its failure point. The tests were conducted in three directions of fabric (roll direction, 45° direction, and vertical direction). Young′s modulus and Poisson′s ratio were calculated using the average data of three directions before 100% stretching. For the cyclic test and failure test of electrode system, an electrode system that consisted of a gold electrode and copper connector was prepared on a fabric substrate. Silver paint was applied to make a mechanical/electrical connection between the gold electrode and the copper connector. Copper wires (100 μm in diameter) were attached to both edge pads of the Cu connector and the designed pad of the gold electrode to measure their electrical resistance change. Electrical resistance is measured by an inductance-capacitance-resistance (LCR) meter (model 891, BK Precision). For the cyclic stretching test, the electrode system was repeatedly stretched and relaxed at 150 mm/min speed for 1000 cycles. The failure test was conducted with a speed stretching of 50 mm/min on the system up to its electrical failure.

### Imaging-based study of conformal contact

For Silbione-fabric substrate thickness measurement, to measure and compare the thickness of the Silbione-fabric substrate depending on coating condition, Silbione was spin-coated with various coating speeds (500, 1000, 1500, 2000, 2500, and 3000 rpm for 1 min). Each sample was cut into 5 mm–by–10 mm size by razor blade to measure its cross section. Optical image analysis was performed using 3D Surface Profiler (VK-X3000, Keyence). For conformal contact visualization and comparison, to compare the level of conformal contact visually, a Thermo Axia Variable Pressure SEM was used to take images of the microstructure of the skin-attached adhesion layer. As the compared, adhesion layers, thick Silbione (500 rpm spin-coated), thin Silbione (3000 rpm, spin-coated), Ecoflex 00-30, and PDMS are cured on the fabric substrate and placed on human skin replica, which is fabricated by a casting process (EpoxAcast 670 HT, Smooth-On).

### Study of a device′s peeling strength and reusability

For peeling strength measurement and calculation, test adhesive pads had various thicknesses (56, 73, 99, 146, 172, and 250 μm) and were prepared in 30 mm–by–80 mm size. For the peeling strength analysis of the fabric substrate, the fabric substrate was attached to the skin and peeled in the vertical direction with a motorized force tester (ESM303, M5-5, Mark-10). The motorized force tester recorded adhesion force data during the test. The adhesive pad was peeled mechanically from the skin at a speed of 50 mm/min. The average peel strength (Newton per millimeter) was calculated by measuring the average load (Newton) of the peel test and dividing it by the width (millimeter) of the bonded pad. Each test was repeated three times to evaluate the average peeling strength. For experimental setup of reusability and method of soap washing, the reusability of the Silbione adhesive pad with the thickness of 250 μm was evaluated by proper cleansing protocols. These test samples were attached to the forehead for 7 hours during sleep and were tested repeatedly for 7 days. For preparing the washed sample, 50 ml of warm water (35°C) was mixed with 5 ml of dish detergent, and the swab was dipped into the solution to soak the prepared detergent solution. To remove residue from the adhesive after each attachment to the forehead, the washed sample was gently brushed with a wet swab for 1 min. Two additional group experiments (unwashed pad after each attach/detach cycle, newly fabricated adhesion pad) were conducted to evaluate the efficacy of the cleansing method. Each sample′s peeling strength for each day was measured by a motorized force tester (ESM303, M5-5, Mark-10). Samples were peeled from the skin at 50 mm/min speed. The peel strength (Newton per millimeter) was calculated by measuring the load (Newton) of the peel test and dividing it by the width (millimeter) of the bonded pad.

### Measurement of work of adhesion

The test consisted of indenting an adhesive layer (Silbione, Ecoflex 00-30, and PDMS) mounted circular polished steel probe into a pig skin that was firmly bonded to a larger circular steel substrate. The probe with the adhesive layer was brought into contact with the skin

Downloaded from https://www.science.org on September 01, 2025

for a minute, and the probe was then retracted at a given speed. The diameter of the probe was 20 mm. The speed of the probe was 0.4 to 40 mm/min. The normal direction peeling force and displacement of the probe were measured by a motorized force tester (stage: ESM303 and gauge: M5-5, MARK-10). The stress-strain curves were plotted from the measured data, and debonding energy of each condition was calculated through it. The work of adhesion of each material was derived by linear fitting of the plot.

### Analysis of skin-electrode contact impedance and SNR

To compare the skin impedance of the electrode with different adhesion layers, gold electrode was placed on various substrates (500 rpm, spin-coated Silbione; 3000 rpm, spin-coated Silbione; Ecoflex 00-30, PDMS). In addition, the control group experiment (gel electrode) was conducted to compare electrode-skin contact impedance. The test was conducted on the forearm area, and the electrode attached area was properly cleaned with skin preparation gel (NuPrep Skin Prep Gel, Weaver and Company). Electrode-skin contact impedance was measured by a skin impedance meter (model 1089NP Checktrode, UFI), which was connected to two electrodes on skin. Normalized value could be achieved by calculating the impedance density of each sample. The effective area of the serpentine gold electrode and gel electrode was measured by 3D Surface Profiler (VK-X3000, Keyence). For the SNR calculation of the sleep data, the noise was assumed to be the data measured before eye closure without any activity, and its amplitude was calculated. For SNR calculation for reusability analysis in Fig. 3F, amplitudes of 100-s-long delta wave during the first N3 stages were calculated from each measurement. The signal amplitudes were averaged for each day of the two separate 7-day measurements. For SNR comparison in Fig. 4B, amplitudes of shown signals at each sleep stage were calculated and averaged. The SNR value was calculated with the following equation: $\mathrm{SNR}_{\mathrm{dB}} = \left[\left(\frac{A_{\mathrm{signal}}}{A_{\mathrm{noise}}}\right)^2\right]$.

### Human subject study

For the clinical study with sleep disorder patients, informed consent was received with a signed consent form before the sleep measurement at the Emory Sleep Center. The study followed the approved protocol from Emory University Institutional Review Board (#00070097). Once the standard PSG setup was placed on the patient by a sleep study technician, our devices were placed on the patient's face so as not to disrupt or overlap with the PSG settings. The sampling rate of PSG was 200 Hz, and the sampling rate of our system was 250 Hz. Data from these patients were used to compare sleep-wake staging between gold-standard PSG and our device using both traditional visual scoring and automated analyses. Healthy control participants provided informed consent with a signed consent form before the at-home study. The experimental protocol was approved by the Georgia Tech Institutional Review Board (#20211). Instructions were given to the subjects regarding how to use the devices by themselves, and the devices were delivered to the subjects to take sleep measurements at home.

### Manual scoring of sleep stages and comparison with PSG

A sleep technologist manually scored the data from the eight clinical study patients measured with both PSG and our system according to the AASM guideline. The patient information data were blinded to the sleep technologist. A device malfunction occurred during the measurement of four patients, and the epochs measured during the malfunction were excluded from the analysis. A total of 2228 epochs were excluded, and 4970 epochs were used for the comparison analysis. The scoring results of the 4970 epochs measured with both PSG and our system from the eight patients were used to calculate the agreement and Cohen's kappa coefficient.

### Data processing

Because of the processing load and for the maximized portability and usability of the wearable system, the signal acquisition and processing scheme is composed of three different electronic devices: (i) wearable facial patches, (ii) portable device (e.g., smartphone, tablet, etc.), and (iii) personal computer (PC). First, the wearable system collects signals from the electrodes on the skin and transmits them to the portable device via Bluetooth for data storage. The portable device simultaneously collects the signals from both forehead and chin devices via BLE. Then, the stored data are transferred to a PC for the complicated signal processing and analysis with CNN, which requires high processing power. All data processing was done with MATLAB. The data measured with our system were first processed by bandpass filtered (from 0.3 to 30 Hz) and notch filtered (from 59 to 61 Hz) to remove various noises, such as drifting, power line noise, background noise, and so on. The cutoff frequencies of the bandpass filter recommended by the AASM guideline were 0.3 to 35 Hz for EEG and EOG and 10 to 100 Hz for EMG. Stop band frequencies of the notch filter were set to 59 to 61 Hz to remove the power line noise with 60 Hz. The filtered data were used to generate a multitaper spectrogram. The recommended parameters from Prerau *et al.* (*43*) were adopted. The frequency range of the spectrogram was set to 0 to 20 Hz. The time-half-bandwidth product was set to 5, and the number of tapers was 9. The window size was set to 5 s, and the step size was 1 s.

### Classification of sleep stages and apnea

The details of machine learning layer information for sleep stage classification appear in tables S1 and S2. Segmented images of the multitaper spectrogram were used for training and evaluation of the CNN-based sleep stage classification and apnea event detection. Sleep data from 32 healthy participants with 15,590 epochs were used to train the CNN-based sleep stage classification. Of the 15,590 epochs, 1883 were W, 685 were N1, 5858 were N2, 4404 were N3, and 2760 were R. Sleep data from 40 apnea patients with 35,927 epochs obtained from Institute of Systems and Robotics, University of Coimbra (ISRUC) public PSG dataset were used to train the CNN-based apnea event detection. Of 35,927 epochs, 829 epochs contained apnea events, and 35,098 epochs were labeled as normal. Sleep data from eight patients with 4970 epochs from our clinical study were used as the test dataset to evaluate the performance of the CNN-based classification models. The labels of sleep stage and apnea events were made on each epoch. For sleep stage label, of the 4970 epochs, 1141 were W, 343 were N1, 2423 were N2, 495 were N3, and 568 were R. For apnea event label, of the 4970 epochs, 196 epochs contained apnea events, and 4774 epochs were labeled as normal. CNN architectures were created according to the form of input data, image-based multitaper spectrograms, drawing influence from earlier models (*45*). The inputs of our CNN were epoch-by-epoch 30-s-long spectrogram images (128 × 128 pixels) of four channels (two EEG and two EOG channels) combined in a square image (256 × 256 pixels). The

Downloaded from https://www.science.org on September 01, 2025

spectrogram image was then resized into 64 × 64 and converted to values between 0 and 1 using normalization. Because the color-image consists of three-color layers (red, green, and blue), every input matrix dimension was a 3D matrix (64 × 64 × 3). The nonlinear activation functions used are the leaky rectified linear unit (leaky ReLU). ADAM (learning rate = 0.002) was used for the optimization of the CNN architecture, and the error was calculated using the cross-entropy loss function. The batch size was set to 16, and the dropout deactivation rate was set to 0.5. Early stopping was used to prevent overfitting by randomly eliminating 20% of the data from the training set and using it as a validation set at the start of the optimization phase. When the validation loss stopped improving, learning rate annealing was performed with a factor of 5. The training was terminated when two successive decays occurred with no network performance improvement on the validation set, and hyperparameters were optimized by random selection method. Resized data were entered into CNN, featuring three layers of 2D convolutions with filters of size 112, 32, and 48, respectively, and kernel size 3 × 3, 3 × 3, and 5 × 5, respectively. A single convolutional cell (Conv_N) consisted of a convolutional layer, one layer of batch normalization, one layer of maximum pooling step with a filter size of 2, and one layer of Leaky ReLu function. Last, the data were flattened and followed by two fully connected layers and passed through a softmax layer and lastly outputted the predicted class (one of the five sleep stages). Details of the structure and parameters of the CNN for sleep stage classification are further summarized in fig. S13 and table S3. For apnea event, an architecture combining CNN and gated recurrent unit (GRU) was created. The inputs of our architecture were epoch-by-epoch 60-s-long spectrogram images (128 × 128 pixels) of four channels (two EEG and two EOG) combined in a square image (256 × 256 pixels). For the 60 s of data included in each spectrogram, 30 s of corresponding epoch, and the next 30 s of the epoch that follows are combined to better capture the sleep fragmentation and enhance the detection performance. The spectrogram image was then resized into 224 × 224 and converted to values between 0 and 1 using normalization. Because the color image consists of three-color layers (red, green, and blue), every input matrix became a 3D matrix (224 × 224 × 3). Resized data were entered into a CNN, featuring two layers of 2D convolutions with filters of size 64 and kernel size 12 × 12. A Conv_N consisted of a convolutional layer, one layer of batch normalization, one layer of ReLU, one layer of max pooling, and a dropout layer. The filter sizes of two max pooling layers were 8 and 4, respectively, and the dropout deactivation rates of two dropout layers were set to 0.5. The data were flattened and followed by one GRU layer (number of hidden units = 9) and one fully connected layer and passed through a softmax layer and lastly outputted the predicted class (either "no event" or "apnea event"). Detailed information of the CNN + GRU architecture was depicted in the fig. S14. For the training of the CNN + GRU architecture, the cross-entropy loss was used as a loss function, and it was optimized using the ADAM optimizer (learning rate = 0.001). Early stopping was used to prevent overfitting by randomly eliminating 20% of the data from the training set and using it as a validation set at the start of the optimization phase. The training was terminated when 10 successive decays occurred with no network performance improvement on the validation set and hyperparameters were optimized by random selection method.

## Supplementary Materials

**This PDF file includes:**

Note S1
Figs. S1 to S16
Tables S1 to S5
Legends for movies S1 to S3

**Other Supplementary Material for this manuscript includes the following:**

Movies S1 to S3

## REFERENCES AND NOTES


1. D. J. Buysse, Sleep health: Can we define it? Does it matter? *Sleep* **37**, 9–17 (2014).
2. K. K. Gulia, V. M. Kumar, Importance of sleep for health and wellbeing amidst COVID-19 pandemic. *Sleep Vigil.* **4**, 49–50 (2020).
3. C. Hublin, M. Partinen, M. Koskenvuo, J. Kaprio, Sleep and mortality: A population-based 22-year follow-up study. *Sleep* **30**, 1245–1253 (2007).
4. S. R. Patel, N. T. Ayas, M. R. Malhotra, D. P. White, E. S. Schernhammer, F. E. Speizer, M. J. Stampfer, F. B. Hu, A prospective study of sleep duration and mortality risk in women. *Sleep* **27**, 440–444 (2004).
5. S. Kwon, H. Kim, W.-H. Yeo, Recent advances in wearable sensors and portable electronics for sleep monitoring. *iScience* **24**, 102461 (2021).
6. M. Hafner, M. Stepanek, J. Taylor, W. M. Troxel, C. van Stolk, Why sleep matters—The economic costs of insufficient sleep: A cross-country comparative analysis. *Rand Health Q.* **6**, 11 (2017).
7. N. F. Watson, Health care savings: The economic value of diagnostic and therapeutic care for obstructive sleep apnea. *J. Clin. Sleep Med.* **12**, 1075–1077 (2016).
8. V. Ibáñez, J. Silva, E. Navarro, O. Cauli, Sleep assessment devices: Types, market analysis, and a critical view on accuracy and validation. *Expert Rev. Med. Devices* **16**, 1041–1052 (2019).
9. E. Guillodo, C. Lemey, M. Simonnet, M. Walter, E. Baca-García, V. Masetti, S. Moga, M. Larsen, H. Network, J. Ropars, Clinical applications of mobile health wearable–based sleep monitoring: Systematic review. *JMIR Mhealth Uhealth* **8**, e10733 (2020).
10. Q. Pan, D. Brulin, E. Campo, Current status and future challenges of sleep monitoring systems: Systematic review. *JMIR Biomed. Eng.* **5**, e20921 (2020).
11. R. B. Berry, R. Brooks, C. Gamaldo, S. M. Harding, R. M. Lloyd, S. F. Quan, M. T. Troester, B. V. Vaughn, AASM Scoring Manual Updates for 2017 (version 2.4). *J. Clin. Sleep Med.* **13**, 665–666 (2017).
12. P. J. Arnal, V. Thorey, M. E. Ballard, A. B. Hernandez, A. Guillot, H. Jourde, M. Harris, M. Guillard, P. Van Beers, M. Chennaoui, The Dreem headband as an alternative to polysomnography for EEG signal acquisition and sleep staging. *Sleep* **43**, zsaa097 (2020).
13. S.-W. Kim, K. Lee, J. Yeom, T.-H. Lee, D.-H. Kim, J. J. Kim, Wearable multi-biosignal analysis integrated interface with direct sleep-stage classification. *IEEE Access* **8**, 46131–46140 (2020).
14. D. J. Levendowski, L. Ferini-Strambi, C. Gamaldo, M. Cetel, R. Rosenberg, P. R. Westbrook, The accuracy, night-to-night variability, and stability of frontopolar sleep electroencephalography biomarkers. *J. Clin. Sleep Med.* **13**, 791–803 (2017).
15. C.-T. Lin, C.-H. Chuang, Z. Cao, A. K. Singh, C.-S. Hung, Y.-H. Yu, M. Nascimben, Y.-T. Liu, J.-T. King, T.-P. Su, Forehead EEG in support of future feasible personal healthcare solutions: Sleep management, headache prevention, and depression treatment. *IEEE Access* **5**, 10612–10621 (2017).
16. S. Shustak, L. Inzelberg, S. Steinberg, D. Rand, M. D. Pur, I. Hillel, S. Katzav, F. Fahoum, M. De Vos, A. Mirelman, Y. Hanein, Home monitoring of sleep with a temporary-tattoo EEG, EOG and EMG electrode array: A feasibility study. *J. Neural Eng.* **16**, 026024 (2019).
17. K. B. Mikkelsen, Y. R. Tabar, S. L. Kappel, C. B. Christensen, H. O. Toft, M. C. Hemmsen, M. L. Rank, M. Otto, P. Kidmose, Accurate whole-night sleep monitoring with dry-contact ear-EEG. *Sci. Rep.* **9**, 16824 (2019).
18. T. Nakamura, Y. D. Alqurashi, M. J. Morrell, D. P. Mandic, Hearables: Automatic overnight sleep monitoring with standardized in-ear EEG sensor. *IEEE Trans. Biomed. Eng.* **67**, 203–212 (2020).
19. A. Sterr, J. K. Ebajemito, K. B. Mikkelsen, M. A. Bonmati-Carrion, N. Santhi, C. Della Monica, L. Grainger, G. Atzori, V. Revell, S. Debener, D.-J. Dijk, M. DeVos, Sleep EEG derived from behind-the-ear electrodes (cEEGrid) compared to standard polysomnography: A proof of concept study. *Front. Hum. Neurosci.* **12**, 452 (2018).
20. D.-H. Kim, N. Lu, R. Ma, Y.-S. Kim, R.-H. Kim, S. Wang, J. Wu, S. M. Won, H. Tao, A. Islam, K. J. Yu, T.-i. Kim, R. Chowdhury, M. Ying, L. Xu, M. Li, H.-J. Chung, H. Keum, M. M. Cormick, P. Liu, Y.-


Downloaded from https://www.science.org on September 01, 2025

W. Zhang, F. G. Omenetto, Y. Huang, T. Coleman, J. A. Rogers, Epidermal electronics. *Science* **333**, 838–843 (2011).
21. H. R. Lim, H. S. Kim, R. Qazi, Y. T. Kwon, J. W. Jeong, W. H. Yeo, Advanced soft materials, sensor integrations, and applications of wearable flexible hybrid electronics in healthcare, energy, and environment. *Adv. Mater.* **32**, 1901924 (2020).
22. H. Kim, Y. S. Kim, M. Mahmood, S. Kwon, N. Zavanelli, H. S. Kim, Y. S. Rim, F. Epps, W. H. Yeo, Fully integrated, stretchable, wireless skin-conformal bioelectronics for continuous stress monitoring in daily life. *Adv. Sci.* **7**, 2000810 (2020).
23. Y. S. Kim, J. Kim, R. Chicas, N. Xiuhtecutli, J. Matthews, N. Zavanelli, S. Kwon, S. H. Lee, V. S. Hertzberg, W. H. Yeo, Soft wireless bioelectronics designed for real-time, continuous health monitoring of farmworkers. *Adv. Healthc. Mater.* **11**, 2200170 (2022).
24. Y. S. Kim, M. Mahmood, Y. Lee, N. K. Kim, S. Kwon, R. Herbert, D. Kim, H. C. Cho, W. H. Yeo, All-in-one, wireless, stretchable hybrid electronics for smart, connected, and ambulatory physiological monitoring. *Adv. Sci. (Weinh)* **6**, 1900939 (2019).
25. Y.-S. Kim, M. Mahmood, S. Kwon, R. Herbert, W.-H. Yeo, in *Nano-, Bio-, Info-Tech Sensors and 3D Systems III*. (SPIE, 2019), vol. 10969, pp. 1096903.
26. K.-I. Jang, S. Y. Han, S. Xu, K. E. Mathewson, Y. Zhang, J.-W. Jeong, G.-T. Kim, R. C. Webb, J. W. Lee, T. J. Dawidczyk, R. H. Kim, Y. M. Song, W.-H. Yeo, S. Kim, H. Cheng, S. I. Rhee, J. Chung, B. Kim, H. U. Chung, D. Lee, Y. Yang, M. Cho, J. G. Gaspar, R. Carbonari, M. Fabiani, G. Gratton, Y. Huang, J. A. Rogers, Rugged and breathable forms of stretchable electronics with adherent composite substrates for transcutaneous monitoring. *Nat. Commun.* **5**, 4779 (2014).
27. Y.-T. Kwon, J. J. S. Norton, A. Cutrone, H.-R. Lim, S. Kwon, J. J. Choi, H. S. Kim, Y. C. Jang, J. R. Wolpaw, W.-H. Yeo, Breathable, large-area epidermal electronic systems for recording electromyographic activity during operant conditioning of H-reflex. *Biosens. Bioelectron.* **165**, 112404 (2020).
28. J.-W. Jeong, W.-H. Yeo, A. Akhtar, J. J. S. Norton, Y.-J. Kwack, S. Li, S.-Y. Jung, Y. Su, W. Lee, J. Xia, H. Cheng, Y. Huang, W.-S. Choi, T. Bretl, J. A. Rogers, Materials and optimized designs for human-machine interfaces via epidermal electronics. *Adv. Mater.* **25**, 6839–6846 (2013).
29. S. Mishra, J. J. Norton, Y. Lee, D. S. Lee, N. Agee, Y. Chen, Y. Chun, W.-H. Yeo, Soft, conformal bioelectronics for a wireless human-wheelchair interface. *Biosens. Bioelectron.* **91**, 796–803 (2017).
30. W.-H. Yeo, Y.-S. Kim, J. Lee, A. Ameen, L. Shi, M. Li, S. Wang, R. Ma, S. H. Jin, Z. Kang, Y. Huang, J. A. Rogers, Multifunctional epidermal electronics printed directly onto the skin. *Adv. Mater.* **25**, 2773–2778 (2013).
31. R. B. Berry, R. Brooks, C. E. Gamaldo, S. M. Harding, C. Marcus, B. V. Vaughn, The AASM manual for the scoring of sleep and associated events. *Rules Terminol. Tech. Specif. Darien Ill. Am. Acad. Sleep Med* **176**, (2012).
32. J. A. Fan, W.-H. Yeo, Y. Su, Y. Hattori, W. Lee, S.-Y. Jung, Y. Zhang, Z. Liu, H. Cheng, L. Falgout, M. Bajema, T. Coleman, D. Gregoire, R. J. Larsen, Y. Huang, J. A. Rogers, Fractal design concepts for stretchable electronics. *Nat. Commun.* **5**, 3266 (2014).
33. K. Lee, X. Ni, J. Y. Lee, H. Arafa, D. J. Pe, S. Xu, R. Avila, M. Irie, J. H. Lee, R. L. Easterlin, D. H. Kim, H. U. Chung, O. O. Olabisi, S. Getaneh, E. Chung, M. Hill, J. Bell, H. Jang, C. Liu, J. B. Park, J. Kim, S. B. Kim, S. Mehta, M. Pharr, A. Tzavelis, J. T. Reeder, I. Huang, Y. Deng, Z. Xie, C. R. Davies, Y. Huang, J. A. Rogers, Mechano-acoustic sensing of physiological processes and body motions via a soft wireless device placed at the suprasternal notch. *Nat. Biomed. Eng.* **4**, 148–158 (2020).
34. N. Rodeheaver, H. Kim, R. Herbert, H. Seo, W.-H. Yeo, Breathable, wireless, thin-film wearable biopatch using noise-reduction mechanisms. *ACS Appl. Elect. Mater.* **4**, 503–512 (2022).
35. N. Rodeheaver, R. Herbert, Y. S. Kim, M. Mahmood, H. Kim, J. W. Jeong, W. H. Yeo, Strain-isolating materials and interfacial physics for soft wearable bioelectronics and wireless, motion artifact-controlled health monitoring. *Adv. Funct. Mater.* **31**, 2104070 (2021).
36. S. Kwon, Y.-T. Kwon, Y.-S. Kim, H.-R. Lim, M. Mahmood, W.-H. Yeo, Skin-conformal, soft material-enabled bioelectronic system with minimized motion artifacts for reliable health and performance monitoring of athletes. *Biosens. Bioelectron.* **151**, 111981 (2020).
37. M. Mahmood, S. Kwon, G. K. Berkmen, Y.-S. Kim, L. Scorr, H. Jinnah, W.-H. Yeo, Soft nanomembrane sensors and flexible hybrid bioelectronics for wireless quantification of blepharospasm. *IEEE Trans. Biomed. Eng.* **67**, 3094–3100 (2020).
38. J. J. Norton, D. S. Lee, J. W. Lee, W. Lee, O. Kwon, P. Won, S.-Y. Jung, H. Cheng, J.-W. Jeong, A. Akce, S. Umunna, I. Na, Y. H. Kwon, X.-Q. Wang, Z. J. Liu, U. Paik, Y. Huang, T. Bretl, W.-H. Yeo, J. A. Rogers, Soft, curved electrode systems capable of integration on the auricle as a persistent brain–computer interface. *Proc. Natl. Acad. Sci.* **112**, 3920–3925 (2015).
39. D. Yao, Y. Qin, S. Hu, L. Dong, M. L. Bringas Vega, P. A. Valdés Sosa, Which reference should we use for EEG and ERP practice? *Brain Topogr.* **32**, 530–549 (2019).
40. H. Danker-hopfe, P. Anderer, J. Zeitlhofer, M. Boeck, H. Dorn, G. Gruber, E. Heller, E. Loretz, D. Moser, S. Parapatics, B. Saletu, A. Schmidt, G. Dorffner, Interrater reliability for sleep scoring according to the Rechtschaffen & Kales and the new AASM standard. *J. Sleep Res.* **18**, 74–84 (2009).
41. Y. J. Lee, J. Y. Lee, J. H. Cho, J. H. Choi, Interrater reliability of sleep stage scoring: a meta-analysis. *J. Clin. Sleep Med.* **18**, 193–202 (2022).
42. L. Tian, B. Zimmerman, A. Akhtar, K. J. Yu, M. Moore, J. Wu, R. J. Larsen, J. W. Lee, J. Li, Y. Liu, B. Metzger, S. Qu, X. Guo, K. E. Mathewson, J. A. Fan, J. Cornman, M. Fatina, Z. Xie, Y. Ma, J. Zhang, Y. Zhang, F. Dolcos, M. Fabiani, G. Gratton, T. Bretl, L. J. Hargrove, P. V. Braun, Y. Huang, J. A. Rogers, Large-area MRI-compatible epidermal electronic interfaces for prosthetic control and cognitive monitoring. *Nat. Biomed. Eng.* **3**, 194–205 (2019).
43. M. J. Prerau, R. E. Brown, M. T. Bianchi, J. M. Ellenbogen, P. L. Purdon, Sleep neurophysiological dynamics through the lens of multitaper spectral analysis. *Physiol. (Bethesda)* **32**, 60–92 (2017).
44. N. Zavanelli, H. Kim, J. Kim, R. Herbert, M. Mahmood, Y.-S. Kim, S. Kwon, N. B. Bolus, F. B. Torstrick, C. S. Lee, W.-H. Yeo, At-home wireless monitoring of acute hemodynamic disturbances to detect sleep apnea and sleep stages via a soft sternal patch. *Sci. Adv.* **7**, eabl4146 (2021).
45. K. Kwon, S. Kwon, W.-H. Yeo, Automatic and accurate sleep stage classification via a convolutional deep neural network and nanomembrane electrodes. *Biosensors* **12**, 155 (2022).

**Acknowledgments**

**Funding:** We acknowledge the support of the Alzheimer's Association (2019-AARGD-NTF-643460) and the National Institutes of Health (R21AG064309). This work was also supported by the IEN Center Grant from the Georgia Tech Institute for Electronics and Nanotechnology. Electronic devices in this work were fabricated at the Institute for Electronics and Nanotechnology, a member of the National Nanotechnology Coordinated Infrastructure, which is supported by the NSF (grant ECCS-2025462). J.-W.J. acknowledges the support of the National Research Foundation of Korea (NRF-2020M3C1B8A01111568 and NRF-2022M3E5E9017759). **Author contributions:** S.K., H.S.K., A.D., and W.-H.Y. designed the research. S.K., H.S.K., K.K., H.K., Y.S.K., S.H.L., Y.-T.K., L.M.T., A.D., and W.-H.Y. performed the research. S.K., H.S.K., K.K., H.K., J.-W.J., L.M.T., A.D., and W.-H.Y. analyzed the data. S.K., H.S.K., L.T., A.D., and W.-H.Y. wrote the paper. **Competing interests:** W.-H.Y. and A.D. are inventors on a pending patent application related to this work, which was filed on 7 September 2022 under U.S. serial no. 63/404,377. L.M.T. is a member of the Board of Directors of the American Academy of Sleep Medicine; any opinions expressed in this work are those of the authors and do not necessarily reflect those of the AASM. The authors declare that they have no other competing interests. **Data and materials availability:** All data needed to evaluate the conclusions in the paper are present in the paper and/or the Supplementary Materials.

Submitted 1 February 2023
Accepted 17 April 2023
Published 24 May 2023
10.1126/sciadv.adg9671

Downloaded from https://www.science.org on September 01, 2025